Tribology International 163 (2021) 107175

Contents lists available at ScienceDirect

Tribology International

journal homepage: www.elsevier.com/locate/triboint

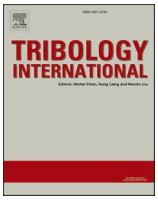

A mathematical model of the erosion process in a channel bend

J.G. Herterich [a,b,*], I.M. Griffiths [c]

[a] School of Mathematics and Statistics, University College Dublin, Belfield, Dublin 4, Ireland
[b] Earth Institute, University College Dublin, Belfield, Dublin 4, Ireland
[c] Mathematical Institute, University of Oxford, Radcliffe Observatory Quarter, Oxford OX2 6GG, UK

ARTICLE INFO

Keywords:
Erosion
Fluid–particle systems
Discrete-to-continuum models

ABSTRACT

We develop a mathematical model for the cumulative erosion of a micro-particle in a channel system. At 90° bends in the system, a particle may deviate from the flow, impact the wall, and erode material. We highlight the case of the eroded material adhering to the particle, growing in size, and thus demonstrate how the damage accumulates exponentially with time. We describe and quantify the statistical nature of the evolution of particle growth and erosion (mass and location). We perform this analysis according to a number of realistic particle concentration distributions: uniform, Gaussian, and bimodal. A bimodal distribution, corresponding to the tubular pinch effect in suspension flows, results in unequal peak zones of erosion due to the flow characteristics.

1. Introduction

Wear is a natural process for materials, arising as a result of interactions between surfaces. In piping systems, wear is often a result of corrosion, releasing solid particles, and erosion, by impact events [1]. Furthermore, as a feedback mechanism, the new surface defects can enhance the corrosion process [2] for a synergistic erosion–corrosion process [3]. Piping systems have a wide range of applications, encompassing household central-heating systems [1,4], coolant systems for small photovoltaic systems [5], and large tokamaks [6]. Pipe failure can be costly and catastrophic, from flooding of the home to termination of large-scale industrial projects. As a result, mathematical models that describe the key mechanisms for pipe wear are essential. The aim of this paper is to develop a mathematical model that describes the dominant contributions to pipe wear, to quantify the process and provide predictions that can act as safeguarding measures to avoid the aforementioned catastrophes.

Erosion is a physical process that induces the wear of materials, with many studies motivated by the oil and gas industry due to the erosive wear of equipment [7]. In piping systems, a ductile metal is impacted by a solid micro-particle in a fluid flow. Cutting and ploughing mechanisms form the basis of deformation and erosion modelling by impact [8]. In this paper, we use the cutting models of Finnie [9,10]. In pipe flow, erosion can occur by solid particles entrained in the flow striking the walls at bends due to their inertia and in straight sections due to turbulent mixing. There are many factors that may influence erosion, including: (i) particle size, shape, and concentration; (ii) surface properties of the pipe material, such as its yield stress; and (iii) flow conditions, which determine the particle velocity and impact angle on the surface. It is observed that in systems where the flow conditions such as direction change rapidly, erosion is more prevalent than in straight pieces of pipes. This applies to pipe bends, turbine blades, and many other industrial processes [9]. An improved energy-based erosion model incorporates surface material properties such as elastic modulus, Poisson's ratio, dynamic pressure, and coefficient of restitution [11].

Particle dynamics in curved pipes has been studied for applications in aerosol science, regarding the deposition of particles [12,13], as well as for erosion studies [14–17,18]. The erosion rate depends on the characteristics of: the individual particles; the suspension as a whole; the flow conditions; the erosion site; and the interaction during impact [14,15]. We note that although particles may erode from multiple sites when transported around a bend, the primary strike erodes more material than secondary strikes [16]. Furthermore, erosion rates decrease with pipe diameter at constant flow conditions [17]. In a gas–solid mixture, particle diameter and the radius of curvature of the bend influence the maximum erosion site [19]. Cheng and Wang [12] provide an analytic solution for particle trajectories in an inviscid flow around a 90° bend, while turbulent flows may be described using k–ϵ turbulent flow models implemented in CFD packages [15] and gas–liquid flows often employ multiphase methods [20]. Chen et al. [21] compare erosion rates for elbow bends in particle-laden flows, with 90° bend resulting in a larger incident angles but at lower velocities than 45° or 60° bends. Mansouri

* Corresponding author at: School of Mathematics and Statistics, University College Dublin, Belfield, Dublin 4, Ireland.
E-mail address: james.herterich@ucd.ie (J.G. Herterich).

https://doi.org/10.1016/j.triboint.2021.107175
Received 12 March 2021; Received in revised form 1 July 2021; Accepted 5 July 2021
Available online 8 July 2021

et al. [18] approximate a low-Reynolds-number flow near the wall to improve overprediction of erosion rates. Smoothed particle hydrodynamics may be used to simulate all damage phenomena [22].

Numerical studies to simulate the deposition and erosion–corrosion processes have been performed for idealised, potential, and parabolic flows in an elbow bend [23–25], a U-bend [26–28], a T-junction [29] and in other more complicated geometries [30]. Erosion–corrosion models usually combine separate models of the two processes [27,30].

For a long and thin geometry, the flow is well described by a Poiseuille flow [31]. For a fully 3D viscous flow in a curved pipe, with the radius of curvature of the bend large compared to the cross sectional radius of the pipe, the primary Poiseuille flow in the direction of the curved axis is complemented by a secondary flow of Dean vortices perpendicular to this axis due to the curvature [32,33], as observed in experiments [34,35]. We neglect the effect of Dean vortices here and consider particle projections in 2D curved channels. A similar flow regime has been applied to viscous aerosol flow with moderate Reynolds numbers and a Stokes drag for the particles dynamics, with an Oseen correction applied for larger particles [23].

Particles entrained in a flow collectively form a concentration distribution. Even in dilute systems, this concentration can have an effect on flow properties such as viscosity [36]. However, for simplicity and to concentrate on the erosion aspect of this system, we neglect such considerations here. However, there are many other physical phenomena that occur in suspension dynamics [37]. The *tubular pinch effect* is an experimentally observed phenomenon whereby neutrally buoyant rigid spherical particles in a low-Reynolds-number Poiseuille flow through a straight circular tube tend to concentrate in an annular region around 0.6 tube radii from the axis in the tube [38,39]. The effect has been simulated numerically for a two-dimensional channel flow, with two Gaussian particle distributions centred approximately halfway between the centre and the edge of the channel [40]. The effect has been observed for Reynolds numbers up to 2400, and occurs irrespective of the position at which the particle enters the tube [38,41]. However, the underlying mechanics that give rise to this phenomenon is still not fully understood [42–44].

In this paper, we derive a mathematical model to explore the erosion process. We consider a specific geometry of a 90° two-dimensional channel bend and study the subsequent erosion. We model the flow of particles in a viscous fluid through a channel bend. We allow the particle to grow in mass as eroded material adheres to a particle that strikes a wall. We limit adhering to a small percentage of impacts since not all material will adhere in all cases [8]. Our simple model shows the effect of particle growth, encompassed with the Stokes number, on the erosion characteristics such as the site of maximum erosion.

We compare results with adhesion of eroded material to the impacting particle for 0%, 2.5%, 5%, 7.5% and 10% of impacts to show the exponential growth in erosion for any amount of adhesion. Without adhesion, a particle causes the same amount of erosion on each impact, leading to a linear increase in eroded material. However, with a growing particle, we explain the exponential growth in erosion in terms of increased inertia, causing a greater amount of erosion with subsequent impacts. Furthermore, an increase in mass alters the trajectory of a particle in the bend, leading to a non-trivial evolution in the location of the increased erosion. The model may be applied to real systems, such as water flowing in copper piping systems, common in household heating systems and industrial coolants. Specifically, the exponentially detrimental erosion effects of a slowly growing particle would be seen in coolant systems designed to be untouched for decades, such as in tokamaks. Such results are prohibitively time consuming to obtain experimentally.

Regardless of whether they operate on small or large scales, the systems discussed all comprise fluid flow in long-and-thin channels (aspect ratio 1/100) under large pressures and flow rates, and hence large velocities (0.5–4 m/s) [4,5,45,46]. Table 1 contains some key parameters and their typical values with reference to a flow of water around a 90° bend with copper walls and a copper oxide corrosive product. Throughout the paper we use these values for reference in presenting results. We quantify erosion based on particle mass and position when entering the bend. We then use the results for a single particle to build a model for the erosion process. We conclude our analysis by discussing how the work presented in this paper can form a foundation for quantitatively predicting the erosion process in industrial settings.

Table 1
Table of notation, nomenclature, and typical values for the channel geometry, flow characteristics, and properties of copper, copper oxide, and water.

Symbol	Description	Typical	Value	Reference
$\hat{L}$	Length of straight section	1–10	m	
$\hat{R}$	Radius of curvature of a bend	5–25	cm	[12,16,47]
$2\hat{a}$	Width of a channel	0.1–5	cm	[12,16,47]
$\hat{a}_p$	Radius of a particle	100	μm	[48]
$\hat{U}_0$	Average flow velocity	0.5–4	m s^{-1}	[4,5,45,46]
$\hat{\rho}_{Cu}$	Density of copper Cu	8940	kg m^{-3}	
$\hat{\rho}_{CuO}$	Density of copper oxide CuO	6310	kg m^{-3}	
$\hat{\sigma}_{Cu}$	Flow stress of copper	10–200	MPa	[49]
$\hat{\mu}$	Dynamic viscosity of water	1×10^{-3}	kg m^{-1} s^{-1}	
$\hat{\rho}$	Density of water	1000	kg m^{-3}	

2. Model

2.1. Setup

We consider the motion of particles in a section of a two-dimensional channel of width $2\hat{a}$ making a 90° bend. Note we use the convention $\hat{*}$ to denote dimensional quantities throughout this paper. In the 90° bend, let the centre of the channel have a radius of curvature $\hat{R}$ and radii of curvature of the inner and outer walls are $\hat{R}-\hat{a}$ and $\hat{R}+\hat{a}$, respectively (Fig. 1). The flow enters and exits the bend from long straight sections, of typical length $\hat{L} \gg \hat{R} > \hat{a}$. Some typical geometrical and physical values for the system are listed in Table 1. The feed flow into the bend has a large Reynolds number $\mathrm{Re} = \hat{\rho}\hat{U}_0\hat{L}/\hat{\mu}$, but for a long and narrow channel (with aspect ratio $\delta = \hat{a}/\hat{L} \ll 1$), the reduced Reynolds number $\delta^2\mathrm{Re}$ is small. Hence a lubrication approximation is appropriate, whereby the transverse length-scale is small compared to the flow direction so that viscous and pressure forces dominate, thus simplifying the problem.

We set fluid and particles to enter the system at cylindrical polar coordinate angle $\theta = 0$, travelling anti-clockwise. We assume that the particles have had time to accelerate to the speed of the flow, at the

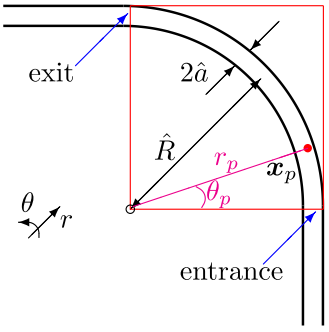

Fig. 1. Schematic of channel geometry at a 90° bend (within box) with radius of curvature $\hat{R}$ and width $2\hat{a}$. Long straight sections lead in and out of the bend. A particle traces a curve with location given in dimensionless variables (see Section 2.2 for details) by $\boldsymbol{x}_p(t) = (r_p(t), \theta_p(t))$ in polar coordinates (r, θ). A closed loop consists of multiple corners joined together by the straight sections.

particular entry point, before entering the bend. The subsequent bend in the channel, together with the inertia of the particle, causes deviation and impact. Fluid and particles exit the system at $\theta = 90^\circ$.

We assume the particles in our model to be spherical and small, of radius $\hat{a}_p \ll \hat{a}$, transported by the fluid tracing a position curve $\hat{\boldsymbol{x}}_p(\hat{t}) = (\hat{r}_p(t), \theta_p(t))$ in cylindrical polar coordinates $(\hat{r}, \theta)$. The particles obey Stokes's law [31], an expression for the frictional or drag force $\hat{\boldsymbol{F}}$ exerted by a steady viscous fluid of velocity $\hat{\boldsymbol{u}}(\hat{\boldsymbol{x}})$ on a small spherical particle of velocity $\mathrm{d}\hat{\boldsymbol{x}}_p/\mathrm{d}\hat{t}$,

$$\hat{\boldsymbol{F}} = 6\pi\hat{\mu}\hat{a}_p\left(\hat{\boldsymbol{u}}(\hat{\boldsymbol{x}}_p) - \frac{\mathrm{d}\hat{\boldsymbol{x}}_p}{\mathrm{d}\hat{t}}\right), \tag{1}$$

where $\hat{\mu}$ is the fluid viscosity. The force is linear in velocity and used in modelling deposition of small particles in flows [12,50]. Non-laminar and higher-Reynolds-number flows usually require a quadratic velocity-dependent drag [51], but we do not consider this here. A flow correction to Poiseuille flow in a curved pipe, via a boundary layer, for a large Reynolds number and small curvature is well established [52].

We note that there will be an additional contribution to the force on the particle due to the fact that it moves at a different velocity to the fluid as it crosses the streamlines, pushing fluid away as it does so. For a particle originating in the centre of the channel, the deviation from the streamlines will be around half the width of the channel and will take place over a quarter pipe length. This so-called added-mass force will therefore contribute an $O(w/\pi R)$ correction to the result. Using the values given in Table 1 indicates that this is typically only around 5%. We therefore neglect the effect here in the interest of clarity of exposition of our study of the cumulative erosion, but note that this could easily be incorporated into our analysis.

We model the transport and impact of individual particles. Particles enter into the flow from the channel walls via corrosion due to oxidation or erosion due to impact. However, corrosion occurs on a much longer timescale compared with the typical time taken for a particle to flow through the system [53]. The released material from impact can either appear as a separate particle entrained in the flow or adhere to the striking particle [8,54]. While the former adds particles that are negligibly small compared to the impacting particle, the latter case is of interest as a cumulative erosion process grows exponentially.

We combine an analysis for individual particles to simulate prescribed concentration distributions. We demonstrate the process with three distributions: a uniform particle distribution, a Gaussian distribution, and a bimodal distribution to represent the tubular pinch effect in a channel [40].

2.2. Nondimensionalisation

In our model, we nondimensionalise the coordinates $\hat{\boldsymbol{x}}$ and $\hat{r}$, particle centre position $\hat{\boldsymbol{x}}_p$ and $\hat{r}_p$, velocity $\hat{\boldsymbol{u}}$, and time $\hat{t}$ variables with

$$\boldsymbol{x} = \frac{\hat{\boldsymbol{x}}}{\hat{a}},\ r = \frac{\hat{r}}{\hat{a}},\ \boldsymbol{x_p} = \frac{\hat{\boldsymbol{x}}_p}{\hat{a}},\ r_p = \frac{\hat{r}_p}{\hat{a}},\ \boldsymbol{u} = \frac{\hat{\boldsymbol{u}}}{\hat{U}_0},\ t = \frac{\hat{U}_0\hat{t}}{\hat{a}}, \tag{2}$$

where $\hat{U}_0$ is the mean flow speed. The dimensionless radius of curvature $R = \hat{R}/\hat{a} = 8$ is such that the inner and outer walls are located at $R - 1$ and $R + 1$, respectively. The domain is specified in cylindrical polar coordinates by the dimensionless radial coordinate $r \in [R - 1, R + 1]$ and angular coordinate $\theta \in [0, \pi/2]$.

We consider particles in the system with initial mass $\hat{m}_0$ and volume $\hat{V}_0$. Particles grow in size, and we nondimensionalise their mass $\hat{m}$, volume $\hat{V}$, and volume eroded $\hat{V}_\mathrm{e}$ with respect to these initial values:

$$m = \frac{\hat{m}}{\hat{m}_0},\ V = \frac{\hat{V}}{\hat{V}_0},\ V_\mathrm{e} = \frac{\hat{V}_\mathrm{e}}{\hat{V}_0}, \tag{3}$$

where $\hat{V} = 4\pi\hat{a}_p^3/3$ and the mass $\hat{m} = \hat{\rho}_p\hat{V}$ with $\hat{\rho}_p$ the particle density.

2.3. Particle motion

The motion of a spherical particle, $\hat{\boldsymbol{x}}_p(\hat{t})$, in a steady fluid flow, $\hat{\boldsymbol{u}}(\hat{\boldsymbol{x}})$, is described by Newton's second law,

$$\hat{m}\frac{\mathrm{d}\hat{\boldsymbol{x}}_p}{\mathrm{d}\hat{t}^2} = \hat{\boldsymbol{F}}, \tag{4}$$

where $\hat{\boldsymbol{F}}$ is the Stokesian drag force defined in (Eq. (1)). Upon applying the nondimensionalisation (Eq. (2)), the governing equation (Eq. (4)) of motion becomes

$$\frac{\mathrm{d}^2\boldsymbol{x_p}}{\mathrm{d}t^2} = \frac{1}{\mathrm{St}}\left(\boldsymbol{u}(\boldsymbol{x_p}) - \frac{\mathrm{d}\boldsymbol{x_p}}{\mathrm{d}t}\right), \tag{5}$$

where St is the Stokes number, a dimensionless number measuring the characteristic time of the particle to that of the flow [55], given by

$$\mathrm{St} = \frac{2\hat{\rho}_p\hat{a}_p^2\hat{U}_0}{9\hat{\mu}\hat{a}} = \frac{\hat{U}_0}{6\pi\hat{\mu}\hat{a}}\left(\frac{4\pi\hat{\rho}_p}{3}\right)^{\frac{1}{3}}\hat{m}^{\frac{2}{3}}. \tag{6}$$

This relation gives a direct correspondence between the particle's inertia and mass. For example, a Stokes number of 2 corresponds to a typical corroded molecule from a copper pipe, such as copper oxide, CuO, with density $\hat{\rho}_{\mathrm{CuO}} = 6310\ \mathrm{kg\ m^{-3}}$, of radius approximately 100 μm in a flow velocity of 1 m/s through a channel approximately 1 cm wide (Table 1).

The impact position and angle not only depend on the flow $\boldsymbol{u}$ and Stokes number St, but also on the initial position $\boldsymbol{x_p}(0)$ and velocity $\mathrm{d}\boldsymbol{x_p}(0)/\mathrm{d}t$ when entering the bend. The particle's entry position is given by

$$\boldsymbol{x_p}(0) = \boldsymbol{x}_0. \tag{7}$$

In a long straight section of channel, it is reasonable to assume that a particle is accelerated to the flow speed itself, so

$$\frac{\mathrm{d}\boldsymbol{x_p}(0)}{\mathrm{d}t} = \boldsymbol{u}(\boldsymbol{x}_0). \tag{8}$$

The governing equations (Eq. (5)), (Eq. (8)) and (Eq. (7)) for particle motion may be expressed in polar coordinates $\boldsymbol{x}_p(t) = (r_p(t), \theta_p(t))$. This leads to a coupled nonlinear second-order system of ordinary differential equations (ODEs) and initial conditions for $r_p(t)$ and $\theta_p(t)$: where $\boldsymbol{x}_0 = (R_0, 0)$ for a radial entry position R_0 at $\theta_p = 0$ (Fig. 1), and the dimensionless angular Poiseuille flow of unit flux is given by

$$\frac{\mathrm{d}^2 r_p}{\mathrm{d}t^2} - r\left(\frac{\mathrm{d}\theta_p}{\mathrm{d}t}\right)^2 = -\frac{1}{\mathrm{St}}\frac{\mathrm{d}r_p}{\mathrm{d}t}, \tag{9a}$$

$$r_p\frac{\mathrm{d}^2\theta_p}{\mathrm{d}t^2} + 2\frac{\mathrm{d}r_p}{\mathrm{d}t}\frac{\mathrm{d}\theta_p}{\mathrm{d}t} = \frac{1}{\mathrm{St}}\left(u_\theta(r_p) - r_p\frac{\mathrm{d}\theta_p}{\mathrm{d}t}\right), \tag{9b}$$

$$\left.\begin{aligned} r_p &= R_0, \\ \theta_p &= 0, \\ \frac{\mathrm{d}r_p}{\mathrm{d}t} &= 0, \\ \frac{\mathrm{d}\theta_p}{\mathrm{d}t} &= \frac{u_\theta(R_0)}{R_0}, \end{aligned}\right\} \text{at} \quad t = 0, \tag{9c}$$

$$u_\theta(r) = \frac{3}{2}[r(2R - r) - (R - 1)(R + 1)]. \tag{10}$$

2.4. Finnie's erosion model

We model the erosion of ductile materials as an attacking cutting mechanism (Fig. 2(a)). The amount of material eroded depends on how deep the particle can cut into the surface. The greater the kinetic energy of the particle, the deeper it cuts into the surface. Although kinetic

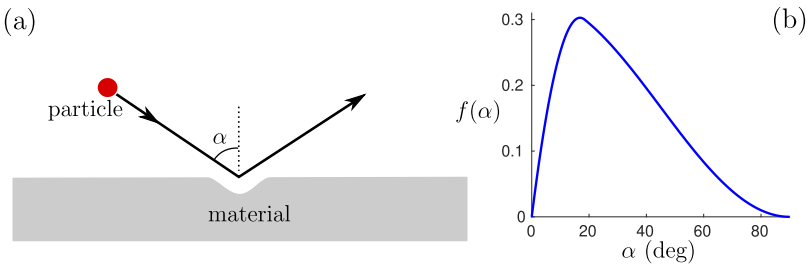

Fig. 2. (a) Schematic of erosion as a cutting mechanism. (b) Impact angle-dependent function $f(\alpha)$, given by Eq. (12) for the volume eroded during impact (Eq. (14)).

energy (proportional to the square of the velocity) is the dominant contribution, particle rotation as it cuts into the surface contributes to an additional volume of material removed (a function of velocity cubed). The combination of the two may, however, be approximated by a single velocity exponent greater than two [48]. The angle of impingement, α, influences the depth a particle can cut into the surface. The stronger the material, with flow stress $\hat{\sigma}$, under bombardment, the less it cuts into the surface. Finnie [9,48] combines these expectations to propose the following model for the volume $\hat{V}_e$ of material eroded when a particle of mass $\hat{m}$ strikes a metal surface with impact speed $\hat{U}_i$:

$$\hat{V}_e = \frac{\lambda \hat{m}\, \hat{U}_i^{\,n} f(\alpha)}{4\hat{\sigma}}. \tag{11}$$

Here, λ is an experimentally determined parameter, incorporating impact characteristics such as fraction of particles cutting in the idealised manner [10,48,56]. In the least material-dependent case [48], λ has been determined to be approximately equal to 0.5 $\mathrm{m}^{2-n}\mathrm{s}^{n-2}$. The flow stress $\hat{\sigma}$ for copper is $\hat{\sigma}_{\mathrm{Cu}} = 10$–$200$ MPa [49]. The index n is typically in the range 2.3–2.4 [48]. However, a larger n is appropriate for a range of materials and suspension properties [14,57], as is found with a data fit to a dimensional analysis of volume eroded [56]. Here we take $n = 2.4$ and $\lambda = 0.5\ \mathrm{m}^{-0.4}\mathrm{s}^{0.4}$. The function f is an experimentally derived function

$$f(\alpha) = \begin{cases} \sin 2\alpha - 3\sin^2\alpha & \alpha < \alpha_0, \\ \frac{1}{3}\cos^2\alpha & \alpha > \alpha_0, \end{cases} \tag{12}$$

accounting for the effect of the angle, α, at which the striking particle impacts relative to the perpendicular direction of the surface (Fig. 2(b)). This cutting mechanism causes maximum erosion for $\alpha = \alpha_0 \approx 18.44^\circ$. Particles colliding perpendicularly with the material ($\alpha \approx 0^\circ$) and particles that graze the surface of the material tangentially ($\alpha \approx 90^\circ$) do not erode any material. Other similar functional forms for f are used [57]. An additional component for plastic or visco-plastic deformation allows for non-zero erosion at high impact angles [58,59]. This modification would affect most significantly the prediction for particles that either strike at a grazing angle or strike close to perpendicular to the channel wall. However, the detrimental effect of grazing strikes will be negligible while strikes that are close to perpendicular to the channel are unlikely to occur in our set-up. (The latter of these cases is confirmed in Fig. 3 (d).) Therefore, while important to acknowledge, such modifications will not have a significant effect on the predictions on the erosive behaviour in our model and so we do not include this effect here.

The impact angle is calculated by simple geometry from the solutions of the particle motion (Eq. (9))

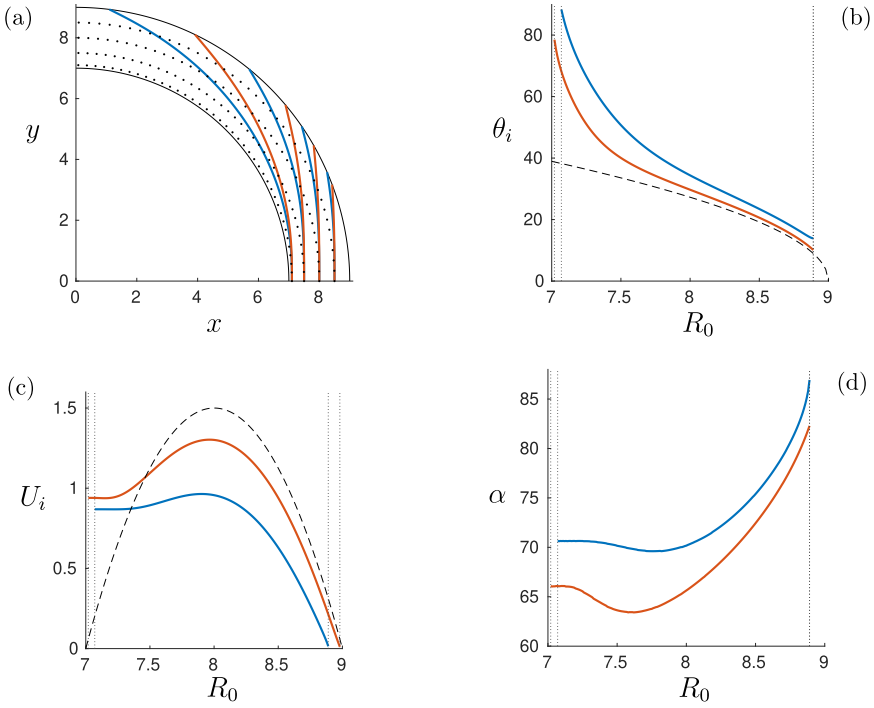

Fig. 3. (a) Numerical solutions of CuO particle trajectories satisfying (Eq. 9) travelling anti-clockwise around a 90° bend in a channel, entrained in Poiseuille fluid flow. The particles enter at $R_0 = 7.1, 7.5, 8.0, 8.5$ and strike the outer channel wall as they deviate from the streamlines (dotted). (b) Angular position θ_i (degrees) of impact for entry position R_0, with limiting angle $\cos^{-1}(R_0/(R+1))$ (dashed) for particles with $\mathrm{St} \gg 1$. (c) Impact velocity U_i (Eq. (15)) for particles entering at R_0, with the velocity at entry given by (Eq. (10)) (dashed). (d) Impact angle α (Eq. (13)) for entry position R_0. Each figure contains results for Stokes numbers $\mathrm{St} = 2$ (blue) and 5 (red). The dotted lines in (b)–(d) represent the limiting entry points where impact occurs (Fig. 5).

$$\alpha = \frac{\pi}{2} - \theta_i + \tan^{-1}\left[\frac{\frac{\mathrm{d}}{\mathrm{d}t}\left(r_p \cos\theta_p\right)}{\frac{\mathrm{d}}{\mathrm{d}t}\left(r_p \sin\theta_p\right)}\right]_{t=t_i}, \tag{13}$$

where $\theta_i = \theta_p(t_i)$ is the angle at impact, and the time derivatives compute the limits for the angle as the moving particle approaches the wall.

Using the nondimensionalisation outlined in Section 2.2, Eq. (11) becomes

$$V_e = S_1\ m\ U_i^n f(\alpha), \tag{14}$$

where recall that for a corroded copper oxide particle $\hat{m} = \hat{\rho}_{\mathrm{CuO}}\hat{V}_0$ and where $S_1 = \lambda\hat{\rho}_{\mathrm{CuO}}\hat{U}_0^n/4\hat{\sigma}_{\mathrm{Cu}}$ and the dimensionless particle impact velocity in polar coordinates is given by

$$U_i = \frac{\mathrm{d}\boldsymbol{r_p}}{\mathrm{d}t}\Big|_{t=t_i} = \sqrt{\left(\frac{\mathrm{d}r_p}{\mathrm{d}t}\right)^2 + \left(r_p\frac{\mathrm{d}\theta_p}{\mathrm{d}t}\right)^2}\ \Big|_{t=t_i}, \tag{15}$$

evaluated at impact time t_i based on particle motion (Eq. (9)).

3. Erosion in a channel bend

We solve for the trajectory, impact, and erosion due to a single particle in a Poiseuille flow around a 90° bend in a channel. We note again that for a secondary strike within the bend the velocity and material eroded on the second strike is reduced [16]. This is also observed in our simulations, even with perfect restitution after the first impact. As such, we model only the first strike. We analyse the system by varying two parameters: the entry position R_0 and Stokes number St.

The governing system (Eq. (9)) does not possess an analytic solution and so we use a Runge–Kutta method to integrate the coupled ODEs. We compare the impact characteristics for a range of parameters, particularly Stokes numbers 2 and 5 for the full range of inlet positions $R_1 < R_0 < R_2$. The two Stokes numbers provide a good comparison in terms of the difference in particle trajectories and impact characteristics, with St = 2 already discussed as typical for a 100 μm CuO particle, and St = 5 for a particle with 60% more mass. Particle deviation from the streamlines towards the outer channel wall increases with Stokes number and decreases with entry point (Fig. 3(a)). The angular position θ_i of impact for all entry points that impact the wall is shown in Fig. 3(b). It is not a linearly decreasing function due to the quadratic nature of the Poiseuille flow, (Eq. (10)). Particles entering the bend on the inner half of the channel must traverse the faster flow region, and hence gain speed. This is an important feature of this system. As the Stokes number increases, the particle motion is less influenced by the flow, and impact occurs at a lower angle (closer to the entrance to the bend), limited by $\cos^{-1}(R_0/(R+1))$. Therefore, as particles grow in mass they subsequently erode from a bend position tending towards that limit.

Impact velocity U_i (Eq. (15)) and cutting angle α (Eq. (13)) are required to quantify the volume eroded (Eq. (14)). The impact velocity (Fig. 3(c)) is lower than its velocity at entry (Poiseuille flow, (Eq. (10)), dashed), except for particles entering close to the inner wall, $R = R_1$. Here, the entry velocity is small but the particle speeds up as it traverses across the faster Poiseuille flow. Particles with a larger Stokes number impact the wall with higher velocities. The cutting angle α decreases with Stokes number (Fig. 3(d)). We have observed that as the Stokes number St, or equivalently the mass m using (Eq. (6)), increases, then so too does the velocity at impact U_i. Further, since the cutting angle α decreases, the function $f(\alpha)$ (Eq. (12)) also increases. These all combine multiplicatively to increase the volume eroded V_e, (Eq. (14)), as shown in Fig. 4 for Cu walls eroded by impacting CuO particles. The volume eroded is maximised for particles entering left-of-centre of the channel (Fig. 4(a)), corresponding to the largest impact velocities (Fig. 3(c)) and smaller cutting angles (Fig. 3(d)). Furthermore, this region of greatest erosion occurs in the channel bend outer wall between 30° and 50°. As the Stokes number increases, the range of impact positions θ_i decreases (Fig. 4(b)).

The volume eroded scales with $S_1 \approx 10^{-5}$ using (Eq. (14)), and thus is small compared with the total particle mass. If this eroded material were to enter into the flow as its own particle, then this would have a Stokes number $\mathrm{St} \ll 1$ and would thus follow the streamlines. However, as discussed, we suppose that in a fraction of cases the eroded material adheres to the impacting particle [8,54], thus increasing the mass (and Stokes number) of that particle. For simplicity we assume the particle remains spherical. After a full cycle in the closed channel system, the now larger particle re-enters the bend. However, if it enters at the same entry point, it does not collide with the wall at the same position θ_i (Fig. 3(b)) because the Stokes number for the motion governed by (Eq. (9)) has increased. An increased amount of material is subsequently eroded at the updated point (Fig. 4) as the additional kinetic energy of a larger particle makes up for any decrease in $f(\alpha)$ (Eq. (14)). This process repeats itself, with long-term cumulative damage being exponential and thus detrimental to the structural integrity of the channel. We model this in the following section.

Note that not all particles impact the wall: there exists a region near the outer wall for which particles that enter in this region never strike the wall of the bend, with limiting entry point R_0*. As a particle

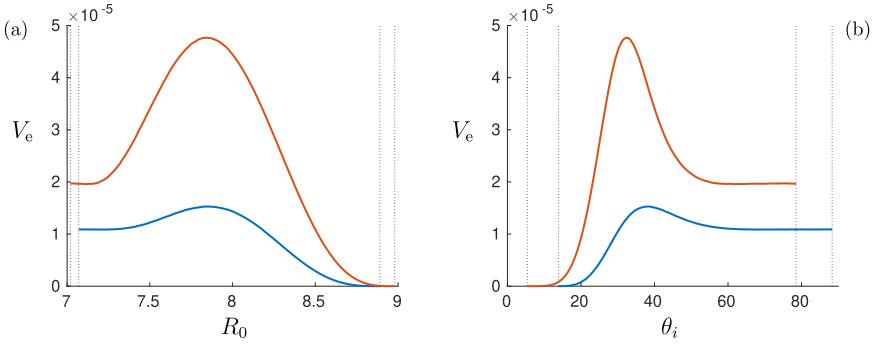

Fig. 4. Volume of Cu eroded by CuO particles against (a) entry position R_0 and (b) the impacting position θ_i using (Eq. (9)). Each figure contains results for Stokes numbers St = 2 (blue) and 5 (red). The volume eroded is scaled by the initial volume of the impacting particle, which depends on the Stokes number, given by (Eq. (6)). The dotted lines represent the limiting entry points where impact occurs (Fig. 5).

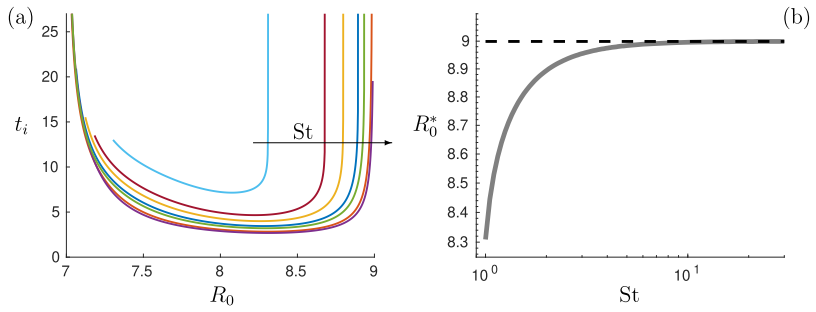

Fig. 5. (a) Impact time t_i by entry point R_0 for Stokes numbers St = 1, 1.25, 1.5, 2, 2.5, 5, and 10. Particles entering the channel near either wall may not impact the outer wall ($t_i \to \infty$). (b) Limiting right-sided entry point $R_0{}^*$ for impact. Cases of $R_0{}^* < R_2 = 9$ correspond to infinite gradients in the curves in (a).

approaches the channel wall, the fluid flow speed is decreasing, and the particle may lose sufficient inertia before striking the wall such that it follows the streamlines. The size of this region depends on the Stokes number (Fig. 5(a)). For St < 0.95, no particles impact the wall as they remain entrained within the flow. When St $= 1$, less than half the entry points results in particle impact with the wall. For St > 2 the effect is negligible as only an extremely narrow range of particle entry points do not impact the wall. For St > 10, impact occurs at all particle entry positions (Fig. 5(b)). Analogously, particles entering the bend near the inner wall ($R_0 - 1$) may not gain sufficient inertia to traverse the channel within the length of the bend, exiting the bend at $\theta = 90^\circ$. Particles entering the bend with lower values of R_0 must travel further (Fig. 3(a)), and may impact the wall at similar times to those that enter at larger values of R_0. This is also a consequence of the Poiseuille flow profile.

4. Particle growth in a closed bend

In the previous section, we related the Stokes number St (Eq. (6)), inlet position R_0, impact position θ_i, and volume eroded V_e (Eq. (14)) during particle impact in a 90° bend. Now we consider the repeated impact of such a particle in a closed piping system. We analyse its rate of growth, where the eroded material adheres to the striking particles. We assume that the shape of the resulting particle is also spherical. This assumption is reasonable since, after many collisions of this type, we expect the shape to be spherical on average. The density of the particle, originally copper oxide with eroded copper adhering, must be updated with each strike. In this section, for illustrative purposes of the discrete and continuum models to be employed later, we assume that all the eroded material adheres to the particle.

We first model the system as a series of discrete impacts in Section 4.1 and then take the continuous limit in which the particle mass grows continuously in time in Section 4.2. The results help quantify the spatial-temporal damage caused to the channel wall. However, in Section 5 we consider a more realistic approach. The assumptions remain valid until such a time that the flow may be classified as a slurry whereby the particle suspension has an effect on the flow properties and particle interactions become significant [37].

4.1. Discrete model

We track the accumulation of mass for one particle with each striking of the channel wall. We suppose that on the i^{th} passage, the particle enters the bend from the same position R_0 with mass m_i and volume V_i and has Stokes number St_i. After each strike the particle increases in mass, volume and Stokes number which are accordingly updated

$$V_{j+1} = V_j + V_{e_j}, \tag{16a}$$

$$\text{St}_{j+1} = \left(\frac{V_{j+1}}{V_j}\right)^{\frac{2}{3}} \text{St}_j, \tag{16b}$$

$$m_{j+1} = m_j + \frac{\hat{\rho}_{\text{Cu}}}{\hat{\rho}_{\text{CuO}}} V_{e_j}, \tag{16c}$$

where V_{e_j} is the volume eroded at strike j (if it does impact the wall). The volume eroded V_{e_i}, given by (Eq. (14)), is dependent on the mass, and hence increases with the Stokes number (Eq. (6)).

4.2. Continuous model

The increase in volume observed after each strike compared with the volume of the particle before impact is small, $\mathcal{O}(S_1) = \mathcal{O}(10^{-5})$ (Fig. 4). We thus consider these increases as infinitesimal to allow us to model the process continuously.

We substitute for V_{e_j} using (14) in (16c) to give

$$\frac{m_{j+1} - m_j}{S_1} = \frac{\rho_{\text{Cu}}}{\rho_{\text{CuO}}} m_j U_i^n f(\alpha). \tag{17}$$

Taking the limit $S_1 \to 0$ allows us to identify the left-hand expression as a continuous derivative $\mathrm{d}m/\mathrm{d}t$ where the timescale t is connected to the discrete model by the fact that $t = S_1$ after one strike. We then obtain an ordinary differential equation describing the growth over the erosion timescale:

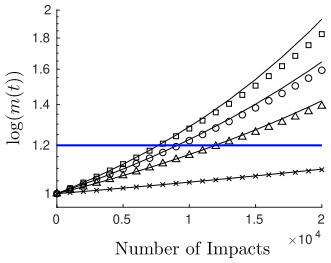

Fig. 6. Particle growth $m(t)$ on a log scale over 20,000 impacts, showing a greater than exponential rate. Growth via the discrete model (Eq. 16) with R_0 = 7.5 (∘), 8 (□), 8.25 (△), and 8.5 (×) and corresponding continuous model (Eq. 18) (solid) begin to diverge after an approximate 20% (horizontal line) growth in mass.

$$\frac{\mathrm{d}m}{\mathrm{d}t} = \frac{\rho_{\mathrm{Cu}}}{\rho_{\mathrm{CuO}}} m U_i(m)^n f(m), \tag{18}$$

where we the impact velocity U_i and the function f are functions of m that we determine numerically (see Figs. 3(c) and 3(d) respectively).

4.3. Comparison

We compare the discrete (Eq. (16)) and continuous (Eq. (18)) models according to Algorithm 1 (below). We implement both models over 20,000 impacts, and observe good agreement before they diverge after a 20% increase in mass, regardless of inlet position (Fig. 6). The number of strikes after which this occurs depends on the inlet position R_0.

Algorithm 1. Calculating particle growth via the discrete (Eq. (16)) and continuous (Eq. (18)) models.

Input: Particle with initial Stokes number St = 2 and entry position R_0
1: **for** each impact **do**
2: Solve particle dynamics system (Eq. (9))
3: Determine volume eroded V_e (Eq. (14)) and erosion site θ_e
4: Determine mass $m(t)$ of particle for discrete (Eq. (16))/continuous (Eq. (18)) models
5: Update Stokes number (Eq. (6))
6: **end**
Output: $m(t)$

Moreover, we observe a dramatic difference in growth depending on entry position R_0. This is a result of the Poiseuille flow (Eq. (10)). Particles entering with $R_0 < R$ traverse the faster fluid and speed up before impact with the outer wall compared to those entering with $R_0 > R$ (see Fig. 3c). Those higher speeds results in greater erosion (Eq. (14)). However, as particles loop around a closed system, they do not enter the same bend at that same entry point. This necessarily means a growth rate that must be averaged over entry positions. We address this in the next section.

5. Statistics of a single particle

5.1. Inlet distributions

In general, a particle suspension entering a channel bend will be well mixed according to a probability distribution of inlet positions, R_0, say $g(R_0)$, where $g(R_0)$ satisfies the required probability constraint,

$$\int_{R-1}^{R+1} g(R_0)\, \mathrm{d}R_0 = 1. \tag{19}$$

In this section, we simulate the recurring entry of a particle into a bend where now each return and re-entry of the particle is at a different location according to g. This more realistic situation lends itself to a statistical description of the erosion caused by an individual particle over a long time in the channel. Again, the particle may impact the wall and erode mass. That mass may either adhere to the particle so that it grows in mass, for a fraction χ of impacts. Otherwise it enters the flow and, as a relatively small mass, follows the streamlines (Fig. 4) and thus does not contribute further to the erosion. However, for each simulation of a particle entering the bend, we use a random number generator to determine the subsequent entry position R_0 on each cycle according to the inlet location distribution $g(R_0)$. We calculate the impact position and mass eroded at each cycle using the discrete model (Eq. (16)) for greater accuracy. We use a uniform random number to determine if this impact is one of the fraction χ that results in adhesion to the impacting particle, and hence a growing particle. We simulate 250,000 cycles, representing the long-term evolution within a sealed coolant system, and perform this analysis for many particles. If a particle does not strike the wall, no erosion occurs. We determine the statistical distribution of impact locations, volume eroded by a particle, and particle growth. The process is summarised in Algorithm 2 (below). As such, we determine an average of the dynamics of erosion caused by a single particle: mass eroded; location of erosion; and particle growth. With this statistical representation of erosion due to a single particle from a distribution, the erosion caused by many particles from a suspension can be determined by scaling up the results to many particles as they are released into the system. Furthermore, we compare the influence of different levels of eroded material adhering to the particle.

Algorithm 2.

Input: Particle with Stokes number St = 2
1: Bend entry position randomised from a distribution g (Eq. (20))
2: Solve particle dynamics system (Eq. (9))
3: Record the cumulative volume eroded V_e (Eq. (14)) and erosion site θ_e with 1 degree bins
4: Use a uniform random number to determine if each impact is one of fraction χ that results in eroded material adhering to the impacting particle
5: If particle growth occurs, update Stokes number (Eq. (6))
6: Repeat Steps 1–5 with entry position for growing particle randomised from the same distribution for 250,000 entries
7: Repeat Steps 1–6 for M different particles
Output: Statistics on location and volume of material eroded by a growing particle

We consider three distributions g – uniform, normal, and bimodal (*tubular pinch effect*) – for illustration of the differing effects on the erosion of the channel wall:

$$g = \left\{ \begin{array}{ll} \mathscr{U}(R_0) = \dfrac{1}{2}, & \text{Uniform} \\ \mathscr{N}(R_0,\nu) = \dfrac{\mathrm{e}^{-(R_0-R)^2/2\nu^2}}{\displaystyle\int_{R-1}^{R+1} \mathrm{e}^{-(R_0-R)^2/2\nu^2}\,\mathrm{d}R}, & \text{Gaussian} \\ \mathscr{B}(R_0,q,\nu) = \dfrac{\mathrm{e}^{-(R_0-R+q)^2/2\nu^2} + \mathrm{e}^{-(R_0-R-q)^2/2\nu^2}}{\displaystyle\int_{R-1}^{R+1} \mathrm{e}^{-(R_0-R+q)^2/2\nu^2} + \mathrm{e}^{-(R_0-R-q)^2/2\nu^2}\mathrm{d}R}, & \text{Bimodal.} \end{array} \right\} \tag{20}$$

Here, $\mathscr{U}(R_0)$ is the uniform distribution for all entry points, $\mathscr{N}(R_0,\nu)$ is the Gaussian normal distribution centred in the middle of the channel with variance ν and $\mathscr{B}(R_0,q,\nu)$ is a bimodal distribution given by two Gaussian distributions, both with variance ν, centred at a distance q from

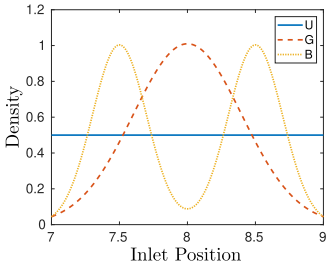

Fig. 7. Particle inlet distributions given by uniform (U), Gaussian (G) with $\nu = 0.4$, and bimodal (B) with $\nu = 0.2$ and $q = 0.5$, as given in (Eq. (20)).

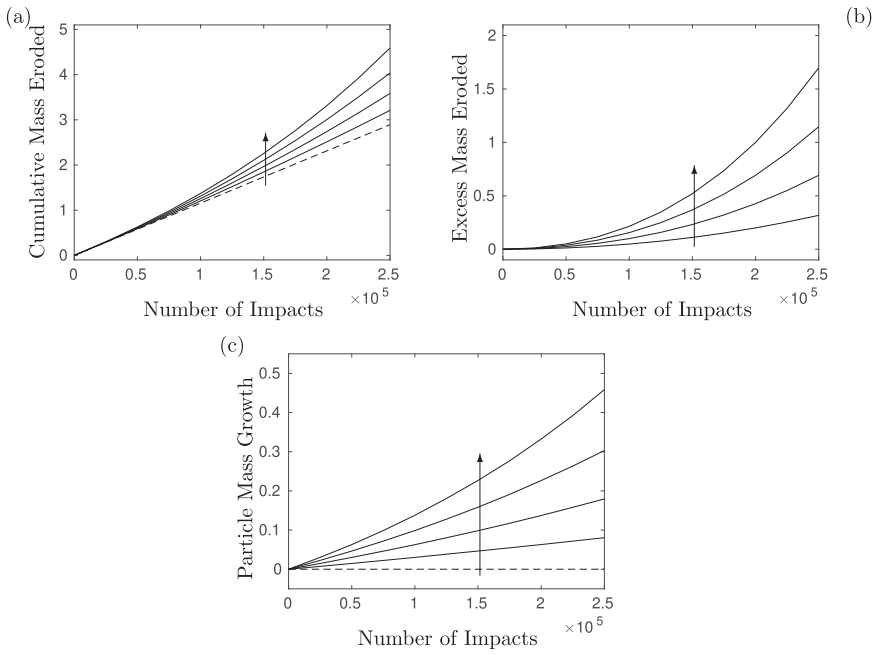

Fig. 8. Evolution of erosion for the uniform inlet distribution (20a). (a) Cumulative mass eroded from the wall for $\chi = 0\%$, 2.5%, 5%, 7.5%, and 10%, with $\chi = 0\%$ the dashed line. (b) Excess mass, relative to $\chi = 0\%$, eroded by a growing particle for $\chi = 2.5\%$, 5%, 7.5%, and 10%. (c) Particle growth for $\chi = 0\%$, 2.5%, 5%, 7.5%, and 10%, with $\chi = 0\%$ the dashed line. The arrows point to increasing χ.

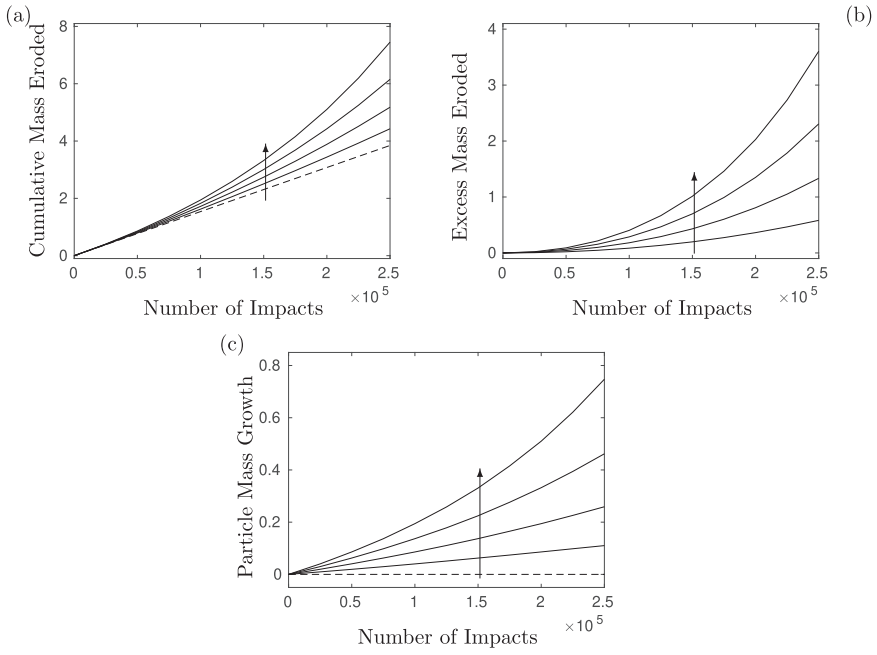

Fig. 9. Evolution of erosion for the Gaussian inlet distribution (20b). (a) Cumulative mass eroded from the wall for $\chi = 0\%$, 2.5%, 5%, 7.5%, and 10%, with $\chi = 0\%$ the dashed line. (b) Excess mass, relative to $\chi = 0\%$, eroded by a growing particle for $\chi = 2.5\%$, 5%, 7.5%, and 10%. (c) Particle growth for $\chi = 0\%$, 2.5%, 5%, 7.5%, and 10%, with $\chi = 0\%$ the dashed line. The arrows point to increasing χ.

the centre of the channel to each wall, i.e., at $R \pm q$. In all simulations we conduct we take $q = 0.5$ and $\nu = 0.4$ for the Gaussian distribution and $\nu = 0.2$ for the bimodal distribution. We illustrate these distributions in Fig. 7.

The location and cumulative mass eroded is averaged over M initially identical particles for 250,000 cycles to obtain the statistics representing the erosion capabilities of a single particle. We consider the average statistics for $M = 20$, with a normed relative error of $\mathcal{O}(10^{-3})$ in mass eroded between $M = 20$ and $M = 21$. The probability density functions for the impact location of a striking particle, for each inlet distribution function (Eq. (20)) as the particle grows in size. We first discuss total cumulative erosion over the whole bend and particle growth, and later analyse the evolution of the distribution of impact locations as an impacting particle grows. We consider the cases of eroded material adhering to the impacting particle for $\chi = 0\%$, 2.5%, 5%, 7.5%, and 10% of cases.

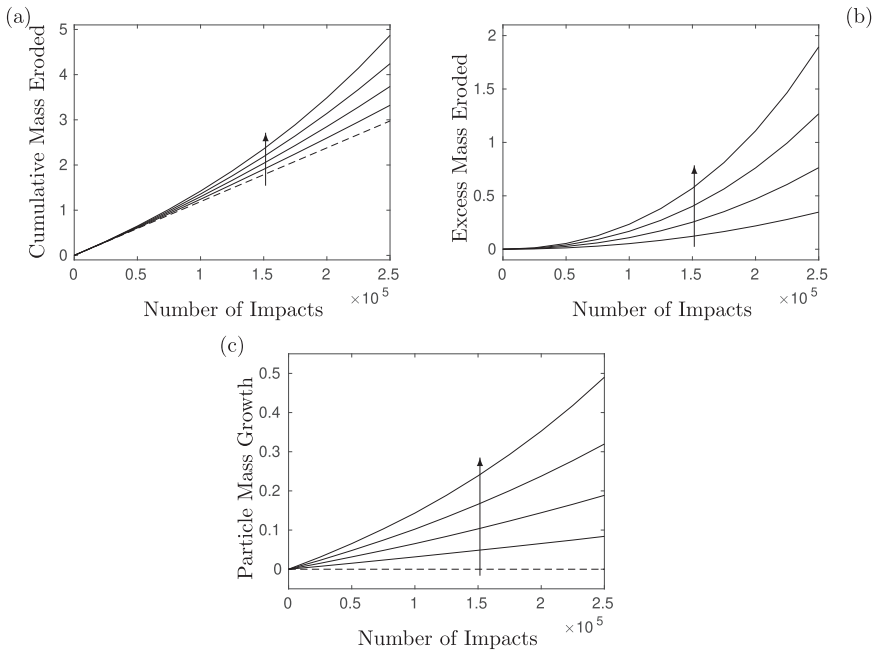

Fig. 10. Evolution of erosion for the bimodal inlet distribution (20c). (a) Cumulative mass eroded from the wall for $\chi = 0\%$, 2.5%, 5%, 7.5%, and 10%, with $\chi = 0\%$ the dashed line. (b) Excess mass, relative to $\chi = 0\%$, eroded by a growing particle for $\chi = 2.5\%$, 5%, 7.5%, and 10%. (c) Particle growth for $\chi = 0\%$, 2.5%, 5%, 7.5%, and 10%, with $\chi = 0\%$ the dashed line. The arrows point to increasing χ.

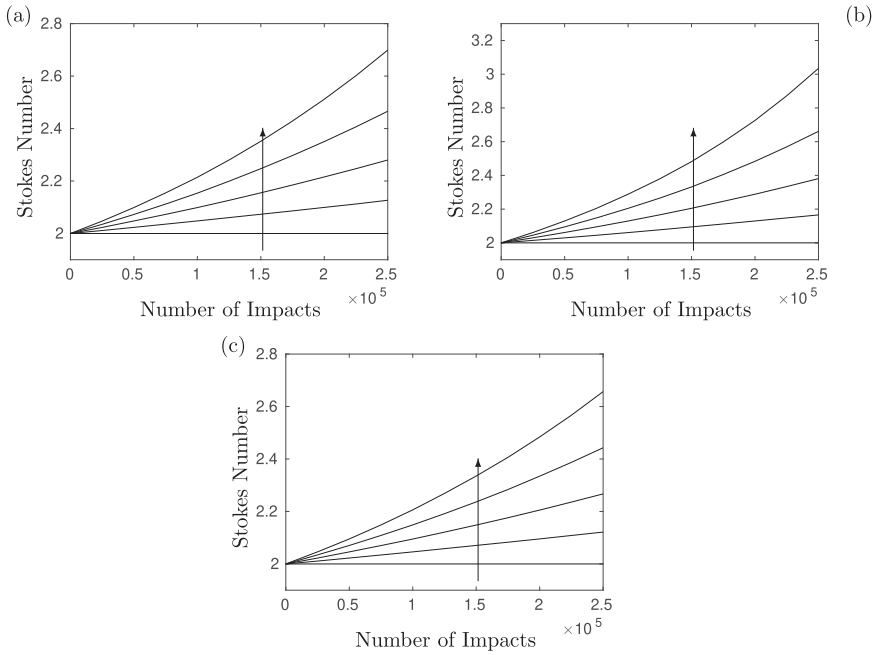

Fig. 11. Growth of Stokes number for (a) uniform, (b) Gaussian, and (c) bimodal distributions (20). The arrows point to increasing $\chi = 0\%$, 2.5%, 5%, 7.5%, and 10%.

5.2. Cumulative erosion and growth

We simulate Algorithm 2, obtaining the statistics for erosion by a single particle. The cumulative mass eroded from the channel wall by one particle grows to many times the initial particle mass over 250,000 impacts (Figs. 8(a), 9(a), 10a). The cumulative mass grows linearly with strikes for $\chi = 0\%$, but exponentially when $\chi > 0\%$. The ranges for mass eroded after 250,000 impacts for $\chi \in [0,10]\%$ are: [3.0, 4.9] for the uniform case, [3.8, 7.5] for the Gaussian case, and [2.9, 4.6] for the bimodal case.

We see the exponential growth more clearly through the excess erosion relative to $\chi = 0\%$ in the system. Adhesion of eroded material to the impacting particle is significant (Figs. 8b, 9(b), 10b). The ranges for excess mass eroded after 250,000 impacts for $\chi \in [2.5, 10]\%$ are: [0.35, 1.9] for the uniform case, [0.58, 3.6] for the Gaussian case, and [0.32, 1.7] for the bimodal case. In fact, the exponential growth of $A\exp\lambda t$ is such that the amplitude A has a strong dependence on χ and the growth rate λ has weak dependence on χ.

The particle mass grows due to adhesion of eroded material (Figs. 8c, 9(c), 10c). The ranges for particle mass growth after 250,000 impacts for

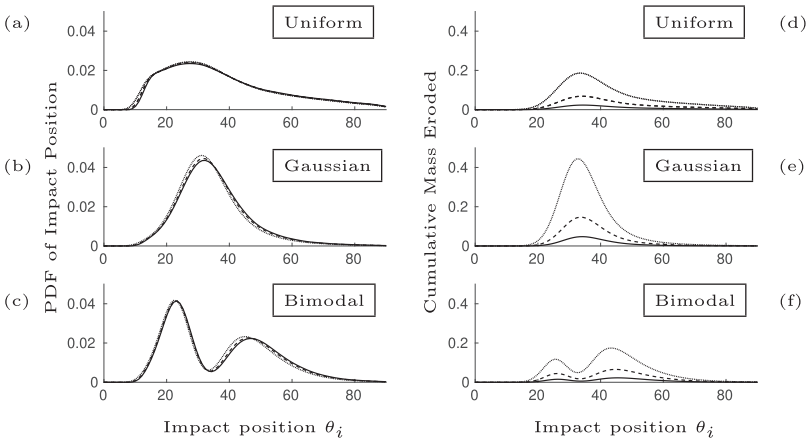

Fig. 12. Left panel (a,b,c): probability distribution function (PDF) counting the frequency of impact along the bend by impact position θ_i. Right panel (d,e,f): cumulative mass m eroded as a function of impact position. The solid curves represent 50,000 cycles, dashed curves represent 125,000 cycles, and dotted curves represent 250,000 cycles. Each curve is a statistical representation of the cumulative erosion, in terms of location and mass, by a single particle according to Algorithm 2 with $M = 20$ particles. In the rows, we distinguish the results with entry positions, over 250,000 cycles, taken from the uniform, Gaussian ($\nu = 0.4$), and bimodal ($q = 0.5$, $\nu = 0.2$) distributions (Eq. (20)) respectively. In all simulations, $\chi = 10\%$.

$\chi \in [0,10]\%$ are: [0.49] for the uniform case, [0, 0.74] for the Gaussian case, and [0, 0.46] for the bimodal case. Note that these numbers scale correctly with the excess erosion according to χ.

Qualitatively similar results are observed for the three distributions. However, while the erosion and particle growth rates are similar for the uniform and bimodal distributions, with uniform causing more damage than the bimodal, the Gaussian distribution causes significantly more damage with a faster growth rate. This is a result of the single central peak distribution (Fig. 7) leading to more particles entering the bend in the faster flowing region of the channel (Fig. 3).

Growth in particle mass m is directly related to the Stokes number St, with $\mathrm{St} \sim m^{2/3}$ (6). We observe the Stokes number increasing for all $\chi > 0$ as expected (Fig. 11). It is this relationship between mass and Stokes number that affects the evolution of dynamics (Fig. 3) and erosion amount and location (Fig. 4). We analyse this in the next section.

5.3. Location of impact and erosion

In the previous section, we considered the cumulative effect of erosion in the bend. Here we discuss the details within that, namely the impact frequency and mass eroded by location in the bend. We analyse the evolution of this process with a growing particle.

For brevity and illustrative purposes we consider results for $\chi = 10\%$. We show the probability density function (PDF) of impact locations as the number of impacts increases in Figs. 12(a,b,c). For reference, with $\chi = 0\%$ there would be no change in the PDF. The corresponding statistical time-cumulative mass eroded by location in the bend is shown in Figs. 12(d,e,f), respectively. We use a moving average to smooth the data: the average is computed with a window, a sliding vector of elements, of length 10 about each point representing 1°, and the average is computed with a Gaussian weighting. The results we discuss are qualitatively similar for lower values of χ, but the effects are less pronounced; more impacts are required to observe similar behaviour.

The statistics of the impact position for each inlet distribution (Figs. 12(a–c)) shift to lower values of θ_i as the number of cycles increases, as expected with growing particles (Fig. 3(b)), increasing in mass for $\chi = 10\%$ of impacts in this case. This increases the inertia of the particle, via the Stokes number as discussed in the previous section, so that the particles deviate more from the streamlines as evidenced in Fig. 3(a). The variation, however, is non-trivial and depends on the inlet distribution (Eq. (20)).

Particles entering on the inner half of the channel, with $R_0 < R$, traverse through the faster-flowing fluid (Fig. 3(c)) and are spread out to a larger degree further along the bend (Fig. 3(a,b)) than those entering on the outer half of the channel, with $R_0 > R$. This affects the impact distribution, with a more concentrated impact region for particles entering with $R_0 > R$ than with $R_0 < R$. However, though particles entering with $R_0 < R$ impact with a wider distribution, two additional factors are also present: (i) the aforementioned larger velocity and (ii) the corresponding impact angle α (Fig. 3(d)) so that $f(\alpha)$ (Eq. (12)) is larger. These two factors in fact combine multiplicatively to increase the volume eroded in (Eq. (14)), in accordance with (Eq. (18)). This trade-off in impact frequency and volume eroded dramatically affects the erosion process depending on the inlet distribution.

This trade-off is most easily seen with the bimodal distribution (Fig. 12(c,f)). Two equal peaks in the inlet distribution result in one larger narrow peak and one smaller wide peak in the impact locations. However, more mass is eroded from an impact zone with lower overall frequency but greater impact speed. This feature is not so easily seen in the uniform (Fig. 12(a,d)) and Gaussian (Fig. 12(b,e)) distributions that have a single peak in the probability density of impact positions, though a subtle shift in skewness is present.

The uniform distribution has the most widespread resulting impact angle distribution (Figs. 12(a)), as expected. There is a central peak at $\theta_i = 28^\circ$. This peak does not change as the particle grows and the Stokes number increases. However, about that peak point, the impact distribution shifts to lower values, again as expected. Furthermore, there is an asymmetry about the peak with the frequency of impact higher to the left than right. This is due to the spread of impact angles of particles entering with $R_0 < R$.

The Gaussian distribution produces a narrow peak in impact position (Figs. 12(b)). Overall, this distribution shifts to lower values as the particle grows, with the peak at $\theta_i = 33^\circ$ shifting to 31°. The cumulative mass eroded by position in the bend (Figs. 12(e)) is much greater than the uniform case (Figs. 12(d)) because of the increased frequency of impact, as expected.

The most interesting case is the bimodal distribution. Here the two peaks in inlet particle distribution produce very different impact position distributions (Figs. 12(c)) and cumulative mass erosion (Figs. 12(f)). Particles entering with the inlet bimodal peak at $R = 8.5 > R_0$

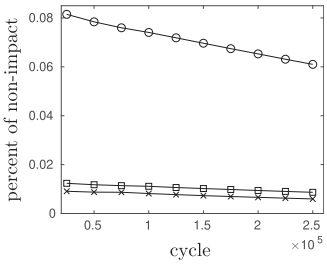

Fig. 13. The percentage of particles that do not impact the walls when passing through the bend as a function of cycle time for the three distributions: uniform (∘), Gaussian (×) with $\nu = 0.4$, and bimodal (□) with $q = 0.5$ and $\nu = 0.2$. This percentage decreases approximately linearly with the greatest rate observed with the uniform distribution. In all simulations, $\chi = 10\%$.

produce a higher narrower impact position peak compared to those entering with the inlet bimodal peak at $R = 7.5 < R_0$. Again this is because of the Poiseuille flow that particles entering at $R < R_0$ must traverse. Over 50,000 impacts, the impact position peaks shift, and that shift is more pronounced in the lower impact position peak: $\theta_i = 23^\circ \rightarrow 22^\circ$ and $\theta_i = 46^\circ \rightarrow 44^\circ$. However, in terms of erosion, the peak with lower frequency has a greater erosion effect. Again, this is attributed to the speed of the particle upon impact.

Note that the peak of cumulative mass erosion by the uniform (Fig. 12(d)) and bimodal (Fig. 12(f)) distributions take similar values, but only the bimodal impact angle distribution has a shift in the peak. This is again because of the location of the entry position corresponding to each impact position peak. Particles in the bimodal system impacting at that peak enter to the left of the channel centre with an associated higher velocity upon impact.

The rate at which particles do not impact the wall decreases approximately linearly with cycle time (Fig. 13), with the largest rate for the uniform distribution. This is due to the increased likelihood (Fig. 7) of a particle entering from a position nearer the walls whereby impact does not occur. Recall in Fig. 5 that the range of inlet positions with no impact occurring decreases as the Stokes number increases.

6. Conclusions and discussion

In this paper, we have modelled particle impact and erosion at a 90° bend in a channel Poiseuille flow. Particles deviate from the flow in the bend and impact the channel wall. The motion and impact properties depend on the parameters of inlet position and Stokes number. We analyse time, location, angle, and velocity of impact based on these parameters. Finnie's model [9,10,48] is used to calculate material erosion. We developed this model to account for the evolving erosion process.

We illustrated the erosion characteristics with statistics based on three inlet distributions: uniform, Gaussian, and bimodal. These represent well-mixed, concentrated, and tubular-pinch distributions respectively. Adhesion of any amount leads to exponential growth in erosion along the bend. The additional exponential erosion is similar for a uniform and bimodal particle distribution, but greater for a Gaussian distribution. Furthermore, we show how the growing particle erodes more material at shifting location distributions. As particles grow in size, the impact site probability density functions shift to lower values due to the change in Stokes number altering the particle trajectories and speeds from the inlet positions. This means that the section of wall most impacted changes with time. However, the rate of erosion does not always follow this pattern. For the bimodal distribution, the influence of the flow on a particle entering the bend about one of the peaks spreads out the corresponding impact site compared to the other peak. However, that same flow increases the particle impact velocity so that more material is eroded throughout the overall less-frequently (more spread out) impacted region.

The methodology outlined here may readily be scaled up to any number of particles, within a dilute limit, incorporating delays to represent the introduction of new particles by corrosive effects. The model we have presented should provide a basis to understand the deleterious effects of erosion in a range of industrial piping systems. We highlight the exponentially detrimental effects of erosion in a closed channel, and appeal to the wider community for experimental or CFD simulations to validate our model. We note that the exponential effects are only observed over a long timescale. As a result, our simple model is a guide for tuning computationally expensive CFD simulations. In addition, our mathematical model is able to quickly provide long-term predictions that would be prohibitively time consuming to obtain experimentally.

Our model may be adjusted or improved in a number of ways for different operating and physical conditions. As mentioned, in the case of non-laminar and higher-Reynolds-number flows, a boundary layer correction [52] in the curved section may be imposed and a quadratic velocity-dependent drag [51] may be applied to the particle transport. For particular materials or extreme operating conditions (impact speed and temperature), Finnie's model may be updated to incorporate a plastic deformation component [58], allowing for erosion at high impact angles [59]. The volume of eroded material adhering to the impacting particle may be adjusted by a factor, either deterministically or stochastically, to capture the practical nature of erosion [8,22,54].

CRediT authorship contribution statement

J.G. Herterich: conceptualization, model development, numerical simulations, writing, reviewing, editing. **I.M. Griffiths:** conceptualization, model development, supervision, reviewing, editing.

Declaration of Competing Interest

The authors declare that they have no known competing financial interests or personal relationships that could have appeared to influence the work reported in this paper.

Acknowledgements

This publication is based on initial work supported by Award No. KUK-C1-013-04, made by King Abdullah University of Science and Technology (KAUST). IMG gratefully acknowledges support from the Royal Society through a University Research Fellowship.

References

[1] Roy S, Coyne JM, Novak JA, Edwards MA. Flow-induced failure mechanisms of copper pipe in potable water systems. Corros Rev 2018;36:449–81.
[2] Zhu Q, Zou L, Zhou G, Saidi WA, Yang JC. Early and transient stages of Cu oxidation: atomistic insights from theoretical simulations and in situ experiments. Surf Sci 2016;652:98–113.
[3] Malka R, Nešić S, Gulino DA. Erosion–corrosion and synergistic effects in disturbed liquid-particle flow. Wear 2007;262:791–9.
[4] Risberg D, Vesterlund M, Westerlund L, Dahl J. CFD simulation and evaluation of different heating systems installed in low energy building located in sub-Arctic climate. Build Environ 2015;89:160–9.
[5] Chow T, He W, Ji J. Hybrid photovoltaic-thermosyphon water heating system for residential application. Sol Energy 2006;80:298–306.
[6] Dell'Orco G, Curd W, Berry J, Chang K, Ferrada J, Gopalapillai B, et al. Design modification and optimization of the ITER cooling water system. Fusion Eng Des 2011;86:15–9.
[7] Parsi M, Najmi K, Najafifard F, Hassani S, McLaury BS, Shirazi SA. A comprehensive review of solid particle erosion modeling for oil and gas wells and pipelines applications. J Nat Gas Sci Eng 2014;21:850–73.
[8] Hutchings I, Winter R, Field JE. Solid particle erosion of metals: the removal of surface material by spherical projectiles. Proc R Soc Lond A Math Phys Sci 1976; 348:379–92.
[9] Finnie I. Erosion of surfaces by solid particles. Wear 1960;3:87–103.
[10] Finnie I. Some observations on the erosion of ductile metals. Wear 1972;19:81–90.
[11] Biswas S, Williams K, Jones M. Development of a constitutive model for erosion based on dissipated particle energy to predict the wear rate of ductile metals. Wear 2018;404:166–75.
[12] Cheng Y, Wang C. Inertial deposition of particles in a bend. Aerosol Sci 1975;6: 139–45.
[13] Tsai C-J, Pui D. Numerical study of particle deposition in bends of a circular cross-section-laminar flow regime. Aerosol Sci Technol 1990;12:813–31.
[14] Javaheri V, Porter D, Kuokkala V-T. Slurry erosion of steel – Review of tests, mechanisms and materials. Wear 2018;408:248–73.
[15] Peng W, Cao X. Numerical simulation of solid particle erosion in pipe bends for liquid–solid flow. Powder Technol 2016;294:266–79.
[16] Njobuenwu DO, Fairweather M. Modelling of pipe bend erosion by dilute particle suspensions. Comput Chem Eng 2012;42:235–47.
[17] P., Zahedi, S., Karimi, M., Mahdavi, B.S., McLaury, S.A., Shirazi, Parametric analysis of erosion in 90 degree and long radius bends, in: ASME 2016 Fluids Engineering Division Summer Meeting collocated with the ASME 2016 Heat Transfer Summer Conference and the ASME 2016 14th International Conference on Nanochannels, Microchannels, and Minichannels, American Society of Mechanical Engineers Digital Collection, pp. 1–11.
[18] Mansouri A, Arabnejad H, Karimi S, Shirazi SA, McLaury BS. Improved CFD modeling and validation of erosion damage due to fine sand particles. Wear 2015; 338:339–50.

[19] Pei J, Lui A, Zhang Q, Xiong T, Jiang P, Wei W. Numerical investigation of the maximum erosion zone in elbows for liquid-particle flow. Powder Technol 2018; 333:47–59.
[20] Zahedi P, Zhang J, Arabnejad H, McLaury BS, Shirazi SA. CFD simulation of multiphase flows and erosion predictions under annular flow and low liquid loading conditions. Wear 2017;376:1260–70.
[21] Chen J, Wang Y, Li X, He R, Han S, Chen Y. Reprint of "Erosion prediction of liquid-particle two-phase flow in pipeline elbows via CFD–DEM coupling method. Powder Technol 2015;282:25–31.
[22] Takaffoli M, Papini M. Material deformation and removal due to single particle impacts on ductile materials using smoothed particle hydrodynamics. Wear 2012; 274:50–9.
[23] Landahl H, Herrmann R. Sampling of liquid aerosols by wires, cylinders, and slides, and the efficiency of impaction of the droplets. J Colloid Sci 1949;4:103–36.
[24] Hacker PT, Brun RJ, Boyd B. Impingement of droplets in 90 degree elbows with fotential flow. National Advisory Committee for Aeronautics; 1953.
[25] Hadžiahmetović H, Hodžić N, Kahrimanović D, Džaferović E. Computational fluid dynamics (CFD) based erosion prediction model in elbows. Teh Vjesn/Tech Gaz 2014;21.
[26] A., Keating, S., Nesic, Particle tracking and erosion prediction in three-dimensional bends, in: 2000 ASME Fluids Engineering Division Summer Meeting, FEDSM2000-11249 Boston, MA, pp. 1–11.
[27] A., Keating, S., Nesic, Prediction of two-phase erosion–corrosion in bends, in: Second International Conference on CFD in the Minerals and Process Industries, pp. 229–236.
[28] Keating A, Nesic S. Numerical prediction of erosion–corrosion in bends. Corrosion 2001;57:621–33.
[29] Vigolo D, Griffiths IM, Radl S, Stone HA. An experimental and theoretical investigation of particle–wall impacts in a T-junction. J Fluid Mech 2013;727: 236–55.
[30] Davis C, Frawley P. Modelling of erosion–corrosion in practical geometries. Corros Sci 2009;51:769–75.
[31] Acheson D. Elementary fluid dynamics. Oxford University Press; 1990.
[32] Dean W. The streamline motion of fluid in a curved pipe. Philos Mag 1928;5: 673–93.
[33] Dean W, Hurst J. Note on the motion of fluid in a curved pipe. Mathematika 1959; 6:77–85.
[34] Eustice J. Experiments on stream-line motion in curved pipes. Proc R Soc Lond A 1911;85:119–31.
[35] White C. Streamline flow through curved pipes. Proc R Soc A 1929;123:645–63.
[36] Herterich JG, Griffiths IM, Field RW, Vella D. The effect of a concentration-dependent viscosity on particle transport in a channel flow with porous walls. AIChE J 2014;60:1891–904.
[37] Guazzelli E, Morris JF. A physical introduction to suspension dynamics. Cambridge University Press; 2012.
[38] Segre G, Silberberg A. Behaviour of macroscopic rigid spheres in Poiseuille flow Part 2. Experimental results and interpretation. J Fluid Mech 1962;14:136–57.
[39] Cox RG, Brenner H. The lateral migration of solid particles in Poiseuille flow – I Theory. Chem Eng Sci 1968;23:147–73.
[40] Cho S, Choi H, Yoo J. Direct numerical simulation of fluid flow laden with many particles. Int J Multiphase Flow 2005;31:435–51.
[41] Matas J-P, Morris J, Guazzelli E. Inertial migration of rigid spherical particles in Poiseuille flow. J Fluid Mech 2004;515:171–95.
[42] Di Carlo D, Edd JF, Humphry KJ, Stone HA, Toner M. Particle segregation and dynamics in confined flows. Phys Rev Lett 2009;102:094503.
[43] Hood K, Lee S, Roper M. Inertial migration of a rigid sphere in three-dimensional Poiseuille flow. J Fluid Mech 2015;765:452–79.
[44] Haddadi H, Di Carlo D. Inertial flow of a dilute suspension over cavities in a microchannel. J Fluid Mech 2017;811:436–67.
[45] Zhang J, Li L, He S, Song W, Fu Y, Zhang B, et al. Development of a three-zone transport model for activated corrosion products analysis of Tokamak Cooling Water System. Fusion Eng Des 2016;109:407–10.
[46] Kim SH, Berry JB. Critical design issues of the tokamak cooling water system of ITER's fusion reactor. Fusion Sci Technol 2011;60:156–60.
[47] Njobuenwu DO, Fairweather M, Yao J. Prediction of turbulent gas-solid flow in a duct with a 90° bend using an Eulerian-Lagrangian approach. AIChE J 2012;58: 14–30.
[48] Finnie I. Some reflections on the past and future of erosion. Wear 1995;186–187: 1–10.
[49] Shih M, Yu C, Kao P, Chang C. Microstructure and flow stress of copper deformed to large plastic strains. Scr Mater 2001;45:793–9.
[50] Pui DY, Romay-Novas F, Liu BY. Experimental study of particle deposition in bends of circular cross section. Aerosol Sci Technol 1987;7:301–15.
[51] Parker G. Projectile motion with air resistance quadratic in the speed. Am J Phys 1977;45:606–10.
[52] Smith FT. Fluid flow into a curved pipe. Proc R Soc Lond A Math Phys Sci 1976; 351:71–87.
[53] Wood R, Wharton J, Speyer A, Tan K. Investigation of erosion–corrosion processes using electrochemical noise measurements. Tribol Int 2002;35:631–41.
[54] Hutchings I, Winter R. The erosion of ductile metals by spherical particles. J Phys D Appl Phys 1975;8:8.
[55] Brennen CE. Fundamentals of multiphase flow. Cambridge University Press; 2005.
[56] Wiederhorn S, Hockey B. Effect of material parameters on the erosion resistance of brittle materials. J Mater Sci 1983;18:766–80.
[57] Desale GR, Gandhi BK, Jain S. Development of correlations for predicting the slurry erosion of ductile materials. J Tribol 2011;133:031603.
[58] Oka YI, Okamura K, Yoshida T. Practical estimation of erosion damage caused by solid particle impact: part 1: effects of impact parameters on a predictive equation. Wear 2005;259:95–101.
[59] Liu Z, Wan S, Nguyen V, Zhang Y. A numerical study on the effect of particle shape on the erosion of ductile materials. Wear 2014;313:135–42.